Electronic Supplementary Information (ESI)

A foldable self-healing rocking chair zinc-ion battery using three-dimensional zinc metal-free anode

Jiawei Long[a], Tianli Han[a], Xirong Lin[b], Yajun Zhu[a,c], Jinyun Liu*[,a]

1. Experimental

1.1 Synthesis of $H_2Ti_5O_{11}·xH_2O$/CC

Firstly, 15 mL concentrated hydrochloric acid was slowly poured into 15 mL deionized water (DIW), followed by dropping 0.75 mL tetrabutyl titanate. After 15 min stirring, the suspension was transformed to be apparent. The mixture was poured into a 40 mL Teflon-lined stainless-steel reactor and a piece of carbon cloth (CC, 1 × 2 cm^2) was immersed in the solution under ultrasonicating. The reactor was placed in an oven and hydrothermally reacted at 180 °C for 8 h. After cooled down to ambient temperature, the TiO_2 loaded CC (TO/CC) was washed by water and ethanol and dried at 60 °C in an oven for 12 h.

12 g NaOH was dissolved in 26.6 mL DIW under magnetic stirring. The transparent solution was poured into a Teflon-lined stainless-steel reactor with a piece of TO/CC immersed. The reaction was taken place in an oven at 200 °C for 12 h. After cooling down to room temperature, the product $Na_4Ti_3O_8$/CC (NTO/CC) was flushed by DIW till pH turned to neutral. The product was subsequently encountered an ion exchange reaction after immersed in 20 mL 1 M HCl solution for 36 h, after rinsed by DIW and ethanol and dried at 60 °C in an oven for 12 h, the final product $H_2Ti_5O_{11}·xH_2O$/CC (HTO·xH_2O/CC.) was obtained. The mass loading of TO/CC, NTO/CC and HTO·xH_2O are 2.0, 3.5 and 3.3 mg cm^{-2}, respectively.

1.2 Preparation of hydrogel electrolyte

The hydrogel electrolytes were prepared via *in-situ* photoinitiated radical polymerization. Typically, a certain mass of acrylamide (AM) and 0.3 mg N,N'-methylenebisacrylamide (MBA) were dissolved in 2 mL 1 M $Zn(CF_3SO_3)_2$ liquid electrolyte to form homogeneous solution at room temperature. 10 μL 2-hydroxy-2-methylpropiophenone (HMPP, 97%) was dispersed in the mixture above before poured into a Petri dish. The free-radical polymerization was conducted by ultraviolet

(UV) irradiation for 120 s under 0 °C. The hydrogel with 0.8 g AM was named as PMZ electrolyte.

1.3 Synthesis of $ZnMn_2O_4$ /CC cathode

$ZnMn_2O_4$ (ZMO) as a typical cathode material for Zn-ion battery here was employed to investigated the performance of $HTO{\cdot}xH_2O$/CC anode in Zn-ion full battery. 1 mmol $Zn(CH_3COO)_2{\cdot}2H_2O$ and 2 mmol $Mn(CH_3COO)_2{\cdot}4H_2O$ were dissolved in 30 mL deionized water and magnetically stirred for 10 minutes. Then, 1 mL ammonia aqueous solution (30 wt%) was added and stirred for another 10 minutes. A piece of CC (2.5 × 2.5 cm^2) was immersed into the solution under ultrasonication. The suspension was transferred to a 40 mL Teflon-lined stainless-steel autoclave and kept at 180 °C for 12 h. After cooling down to room temperature, the ZMO/CC was rinsed with deionized water and ethanol for several times then dried at 110 °C overnight. The mass loading of ZMO was 2.8 mg cm^{-2}.

1.4 Characterization

The morphology, structure and composition were investigated on a scanning electron microscopy (SEM, Hitachi S8100, operated at 5 kV), a transmission electron microscopy (TEM, Hitachi HT7700) and a high-resolution transmission electron microscopy (HRTEM, FEI TalosF200x), and X-ray diffraction (XRD, Rigaku SmartLab) with the Cu Kα of 1.5418 Å. X-ray photoelectron spectroscopy (XPS, Escalab 250Xi) was used to analyze the elemental state and all the spectra were calibrate by the binding energy of C1s at 284.8 eV. Thermogravimetry analysis (TGA, TA5500) was employed to measure the content of crystalline water. The PMZ hydrogel was immersed in liquid nitrogen then freeze-dried for 48 h. Fourier transform infrared (FT-IR) spectroscopy (INVENIO IR-21) and Raman spectrometry (Renishaw, inVia) were employed to study the functional groups on fully dried PMZ hydrogels by using commercial PAM as reference.

1.5 Electrochemical measurements

The electrochemical impedance spectra (EIS), linear scan voltammetry (LSV) and cyclic voltammetry (CV) were carried out on an electrochemical workstation (Chenhua, CHI-660e), while the Zn||Zn symmetric and Zn||Cu asymmetric cells analysis were carried out on battery tester (Neware, CT-4008).

Stainless steel (SS, 10 μm) foil was used to construct the sandwiched system for testing the ionic conductivity of electrolytes and calculated according to the equation [1, 2]:

$$\sigma = d/(R*A)$$

where σ stands for the resistivity of ionic conductors (S cm^{-1}), R is the resistance (Ω), A is the contact area of the electrolyte (here is 1 cm^2), and d (cm) is the distance between SS foils, respectively.

LSV analyses were conducted for the electrochemical stability windows by respectively using SS foils as working and counter electrode, and Ag/AgCl (1 M KCl) electrode as reference electrode at a scanning rate of 5 mV s^{-1}.

The stability of the PMZ and liquid electrolytes were also investigated by assembling Zn||Zn symmetric batteries. The cells were tested under different current densities and areal capacities. The Coulombic efficiency (CE) test was performed using Cu foil as working electrode. The cutoff voltage of Zn||Cu half-batteries during charging were set to 1.0 V.

To study Zn^{2+} storage performance, polished Zn foil (1.2 × 2.2 × 0.02 cm^3), PMZ electrolyte (1.2 × 2.2 × 0.4 cm^3) were employed as counter/refernece electrode and electrolyte, TO/CC, NTO/CC and HTO·xH_2O/CC (1 × 2 cm^2) were used as working electrodes to construct sandwiched-like quasi-solid-state batteries. The cells were sealed with aluminum laminated film (ALF) on a vacuum sealing machine.

The capacitive and diffusion-controlled behaviors obey an empirical power law $i=av^b$ and $\log(i) = b\log(v) + \log(a)$, where where i (mA) represents the current, v (mV s^{-1}) stands for the scan rate, a and b are the changeable parameters [3, 4]. While the pseudocapacitive contribution ratios at various sweep rates can be estimated according to the equations: $i(V) = k_1v + k_2v^{1/2}$, where k_1v and $k_2v^{1/2}$ stands non-Faradic (capacitive behavior) and Faradic (diffusion-controlled process) process. The values of k_1 and k_2 can be calculated by transformed the equation to $i(V)/v^{1/2} = k_1v^{1/2} + k_2$ and plotting $i(V)/v^{1/2}$ versus $v^{1/2}$.

Galvanostatic intermittent titration technique (GITT) measurement for HTO·xH_2O/CC and NTO/CC anode were conducted at 100 mA g^{-1} for the investigation of diffusion coefficient and internal reaction resistances (RRs). It was further calculated through Fick's law. The equation is as follow [5, 6]:

$$D_{Li^+} = \frac{4}{\tau\pi}\left(\frac{n_m V_m}{S}\right)^2\left(\frac{\partial E_s}{\partial E_\tau}\right)^2$$

$$RR=\Delta U/(I/m^2)$$

where D_{Li+} stands for diffusion coefficient (cm^2 s^{-1}), τ stands for relaxion time (here is 600 s), n_m (mol) and V_m (cm^3 mol^{-1}) are the amount of anode materials and their molar volume, respectively. ΔU (V) refers to the absolute value of the difference between equilibrium and polarization potentials. I stands for current density, which is relevant to the mass of anode materials.

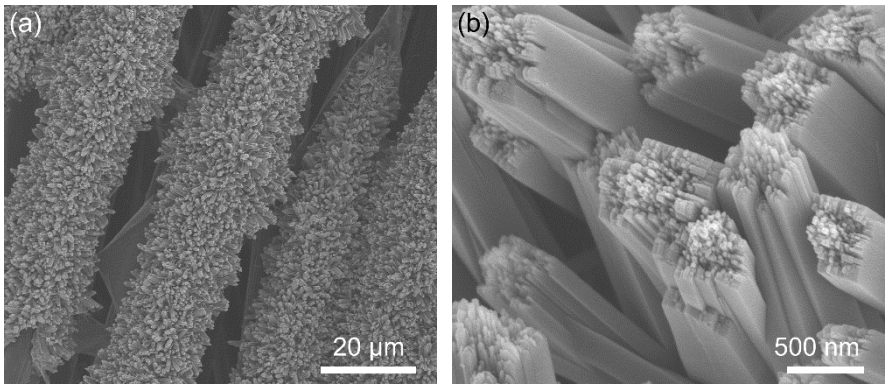

Figure S1. SEM images of TO/CC under various magnifications.

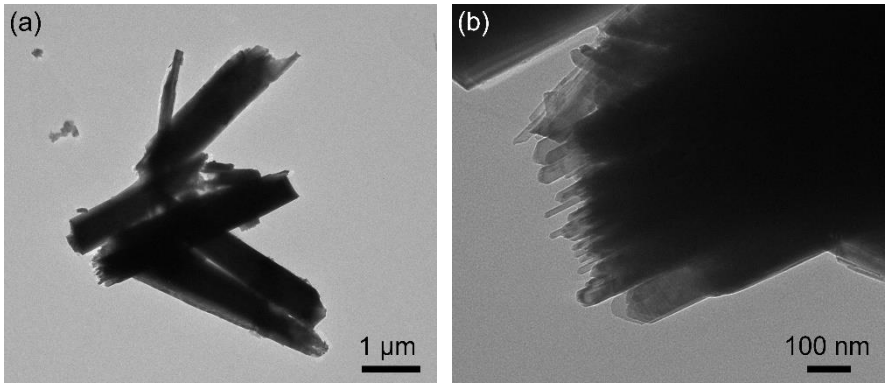

Figure S2. TEM images of TO under different magnifications.

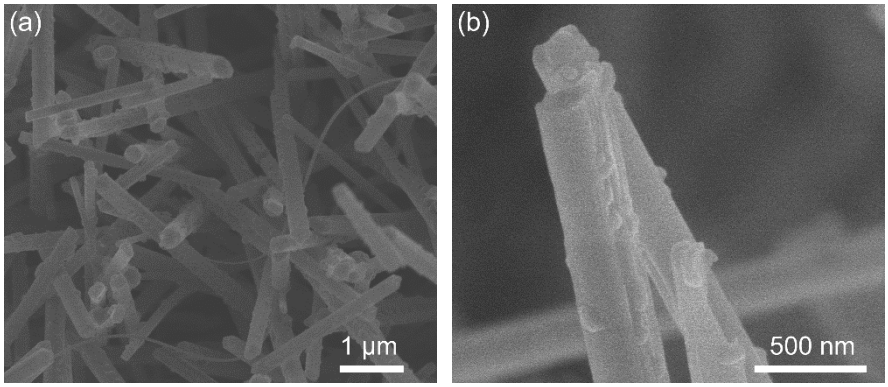

Figure S3. SEM images of NTO/CC under different magnifications.

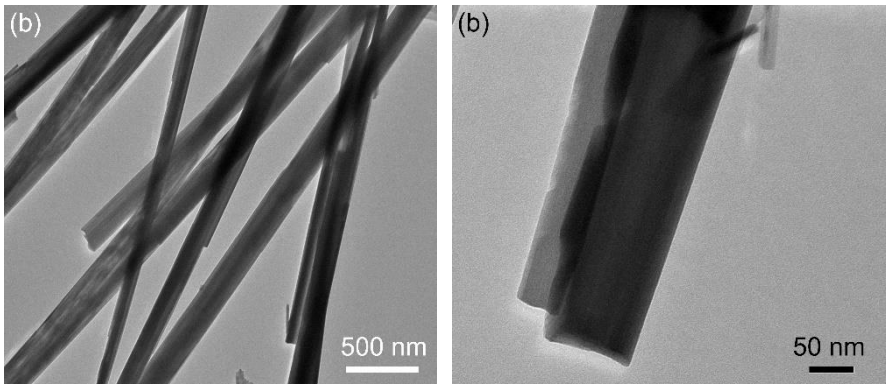

Figure S4. TEM images of NTO under different magnifications.

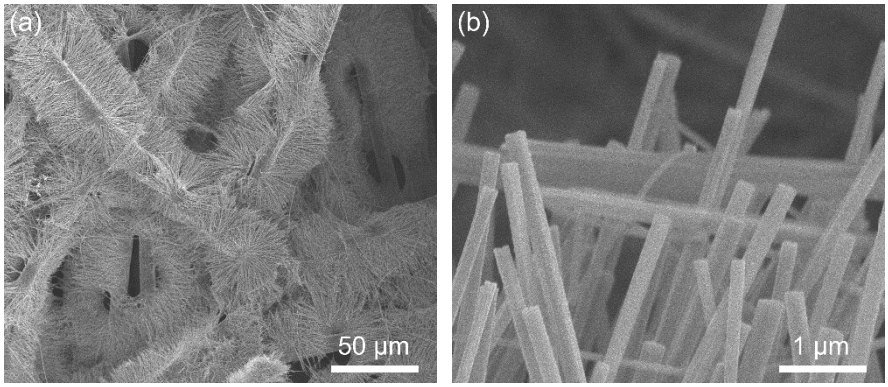

Figure S5. SEM images of HTO·xH_2O/CC under different magnifications.

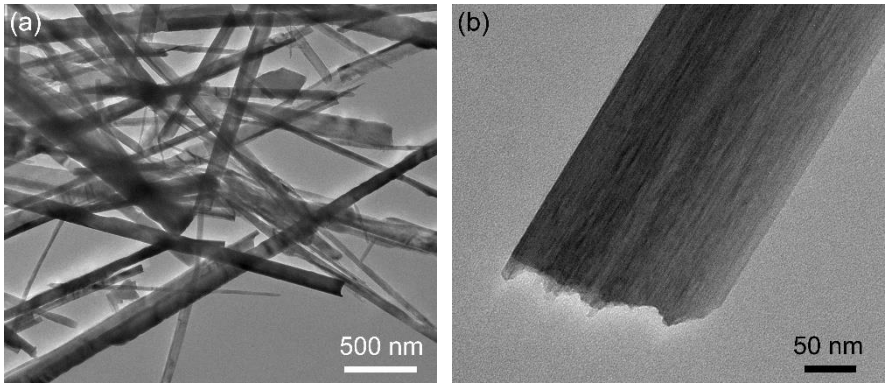

Figure S6. TEM images of HTO·xH_2O under different magnifications.

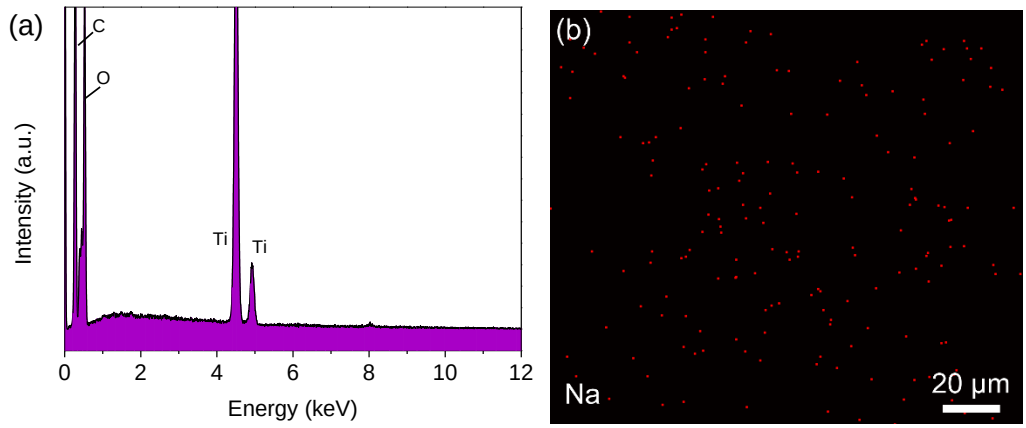

Figure S7. (a) EDS spectrum and of HTO·xH2O /CC. (b) Elemental mapping of Na.

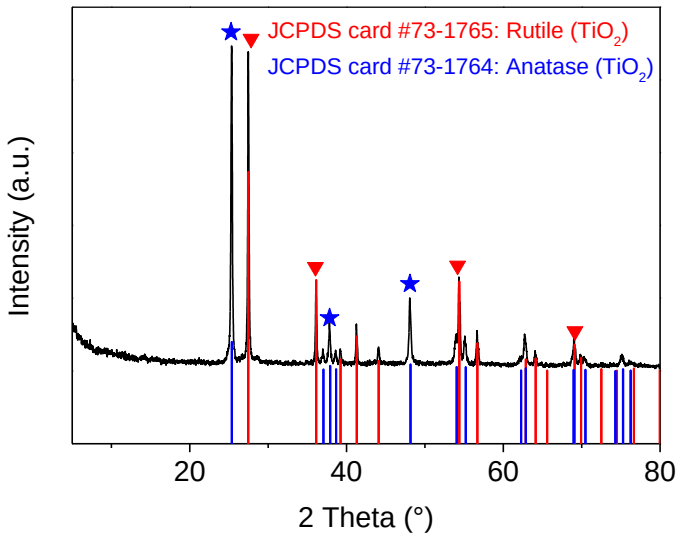

Figure S8. XRD pattern of the residue of HTO·xH2O after TGA test.

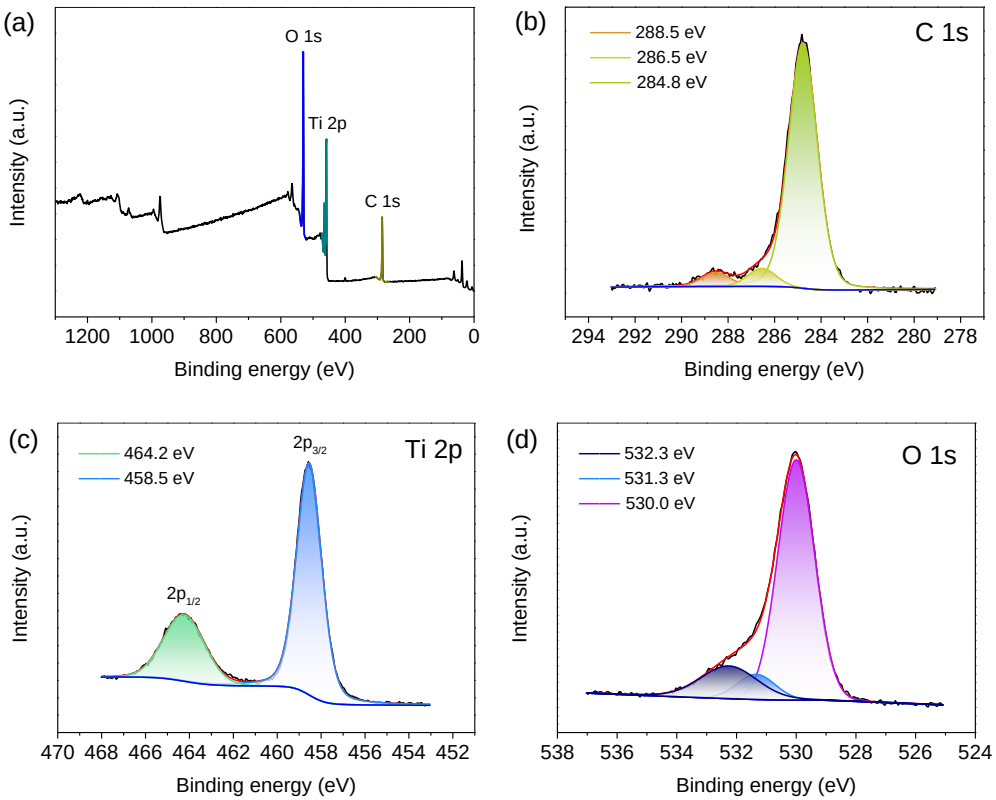

Figure S9. XPS spectrum of HTO·xH_2O /CC. (a) Survey spectrum and high-resolution spectrum of (b) C 1s, (c) Ti 2p and (d) O 1s.

In Figure S9a, C, O and Ti elements are detected on the surface of HTO·xH_2O /CC. All the high-resolution spectra are calibrated via C—C bonds located at 284.8 eV [7], as displayed in Figure S9b. The doublet peaks located at 464.2 and 458.5 eV can be attributed to Ti $2p_{1/2}$ and Ti $2p_{3/2}$, respectively, implying the existence of Ti (IV) [8]. In Figure S9d, there are two peaks centered at 530.0 and 531.3 eV, corresponding to lattice oxygen (Ti—O) and surface adsorption of oxygen (O_{ads}), respectively [9]. While the peak at 532.3 eV is considered as H_2O, indicating the existence of lattice water [10].

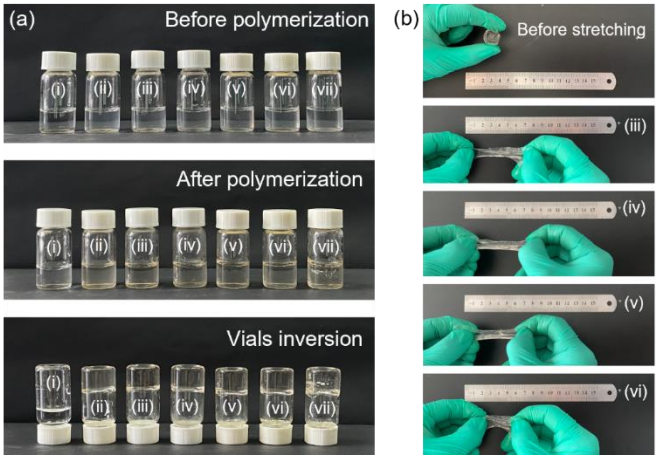

Figure S10. Optical photographs for (a) hydrogels with different masses of AM monomer in 2 mL liquid electrolyte: (i) 0 g, (ii) 0.4 g, (iii) 0.6 g, (iv) 0.8 g, (v) 1.0 g, (vi) 1.2 g, (vii) 1.4 g. (b) Corresponding strain performance.

A series of polyacrylamide (PAM) hydrogels with different masses of AM in 2 mL of 1 M $Zn(CF_3SO_3)_2$ were polymerized under ultraviolet (UV) irradiation. In our study, N,N'-methylenebisacrylamide (MBA) was employed as a crosslinker. In Figure S10a, after polymerization, flowable electrolytes contain the AM mass ≥ 0.6 g transform to semi-solid-state hydrogels and adhere to the glass wall even if the vials are inverted. The hydrogel (Φ=1.7 cm, thickness=0.7 cm) can be elongated for 11 cm (647%), 9 cm (529%), 8.5 cm (500%) and 6 cm (353%) with the AM mass of 0.6, 0.8, 1.0 and 1.2 g, respectively (Figure S10b). Hydrogel become sturdy to be stretched when AM mass raises over 1.4 g.

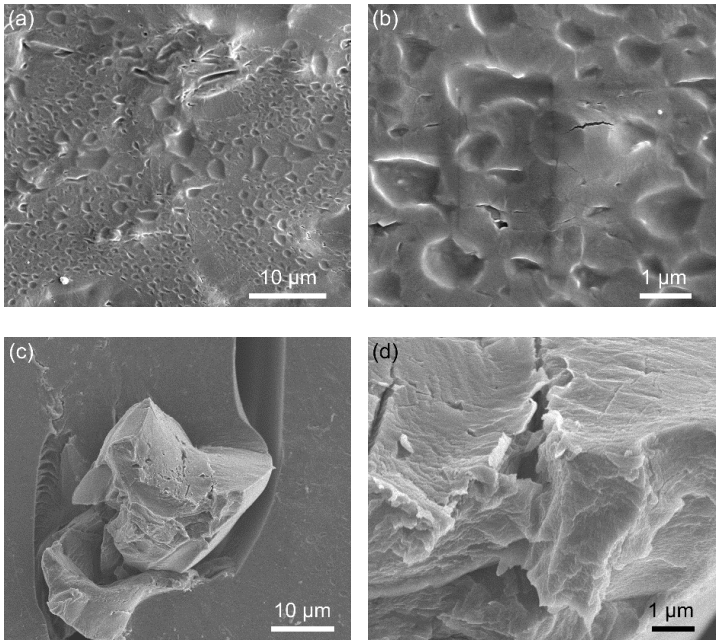

Figure S11. SEM images of freeze-dried hydrogels with different mass of AM monomer in 2 mL liquid electrolyte. (a,b) 0.8 g, (c,d) 1.4 g.

As seen from the SEM images (Figure S11), the freezer-dried hydrogel with AM mass of 1.4 g shows

a dense structure compared to the one of 0.8 g. It is attributed to the cross-linking and bounding of excessive PAM macromolecular skeleton in the hydrogel [11]. When using as electrolyte for AZIBs, the poor adhesion between electrodes and hydrogel electrolyte is detrimental for long-term stability. Therefore, the hydrogel electrolyte with 0.8 g AM additive in 2 mL liquid electrolyte was selected and named as PMZ electrolyte for subsequent studies.

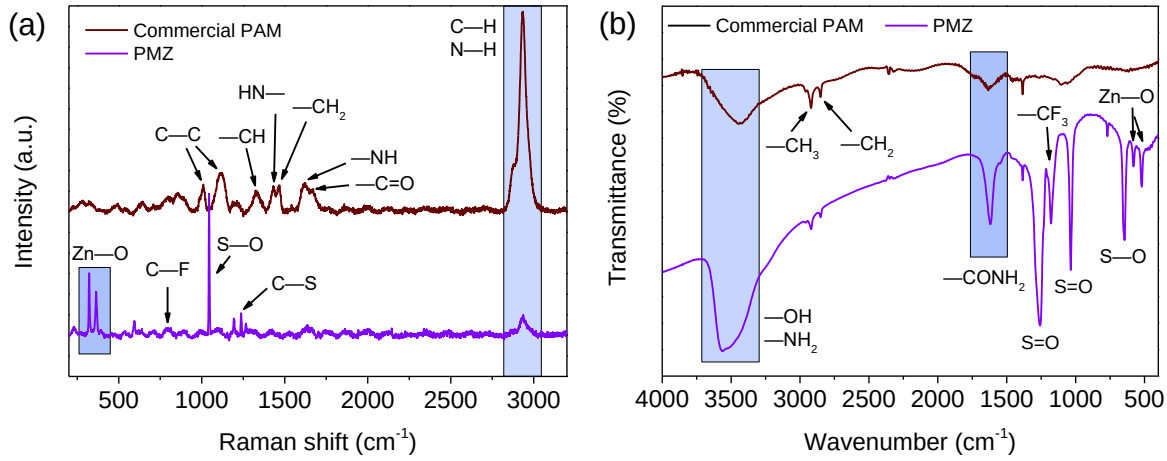

Figure S12. Spectra of commercial PAM and freeze-dried PMZ hydrogel. (a) Raman shift. (b) FTIR spectrum.

Raman spectrum of commercial PAM powders in Figure S11a shows a broad peak located at 2878 and 2935 cm^{-1}, which are ascribed to C–H stretching and N–H stretching vibration [12]. There are two peaks located at 1621 and 1671 cm^{-1}, corresponding to –NH bending and C=O stretching vibration, respectively [13]. A series of peaks at the range of 400 to 1500 cm^{-2} can be attributed to $–CH_2$ bending (1463 cm^{-1}), C–H bending (1325 cm^{-1}), C–C skeletal stretching (1119 and 1010 cm^{-1}) [14-16]. Compared to commercial PAM, there are serial peaks below the Raman shift number of 1500 cm^{-1} for dried PMZ hydrogel. A strong peak depicted at 1045 cm^{-1} can be ascribed to S–O stretching vibration, while the peak at 796 and 1238 cm^{-1} stand C–F stretching and C–S stretching vibration [17, 18]. Two peaks located at 322 and 363 cm^{-1} matches well with Zn–O vibration [19].

FTIR analyses were also conducted to further studied the functional groups in commercial PAM and dried PMZ electrolyte. As seen in Figure S11b, a broad peak located at 3566 cm^{-1} is ascribed to $—NH_2$ stretching and –OH stretching vibration [20]. Doublet peaks at 2926 and 2853 cm^{-1} can be attributed to C–H stretching vibration in $–CH_3$ and $–CH_2$ groups [21]. A typical peak centered at 1617 cm^{-1} stands for $–CONH_2$ stretching vibration [22]. Unlike commercial PAM, there are more peaks between 2000 and 500 cm^{-1} on the IR curve of freeze-dried PMZ hydrogel. Wherein, there are two peaks located at 1258 and 1035 cm^{-1}, corresponding to S=O stretching vibration, while the peak located at 645 cm^{-1} is assigned to S–O stretching vibration [23]. There is a peak at 1178 cm^{-1}, indicating the presence of $–CF_3$ [24]. There is a pair of peaks at 580 and 520 cm^{-1}, corresponding to Zn–O vibration [25].

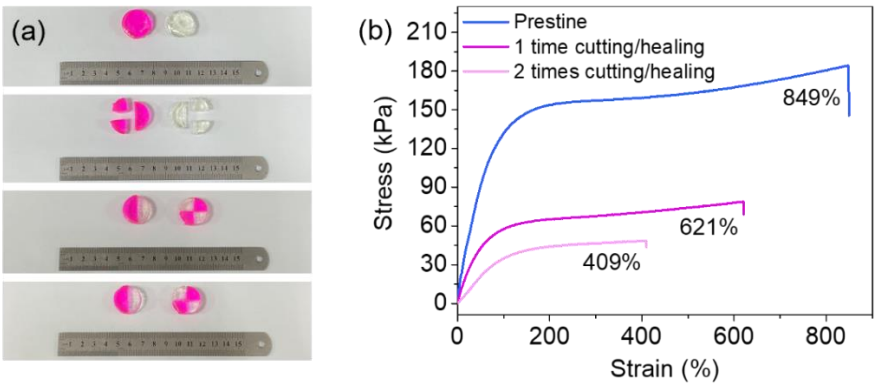

Figure S13. (a) Self-healing performance of PMZ hydrogel electrolyte. (b) Tensile test for the hydrogel after different times of cutting/healing.

For the self-healing tests, rhodamine B-dyed hydrogel and PMZ were cut from the middle and a quarter. After the broken hydrogel connects, they can be well bonded owing to the hydrogen bonds regenerated between amino, carbonyl groups (on PAM skeleton) and water molecules (Figure S12). After standing 30 min, colour osmosis can be observed at the fracture. It is ascribed to the diffusion of the dye molecules. The hydrogels with 1 and 2 times cutting/healing are stretched for 621% and 409%, respectively, compared to the 849% for the intact ones (Figure S13), verifying a good mechanical performance of the post-healed hydrogel.

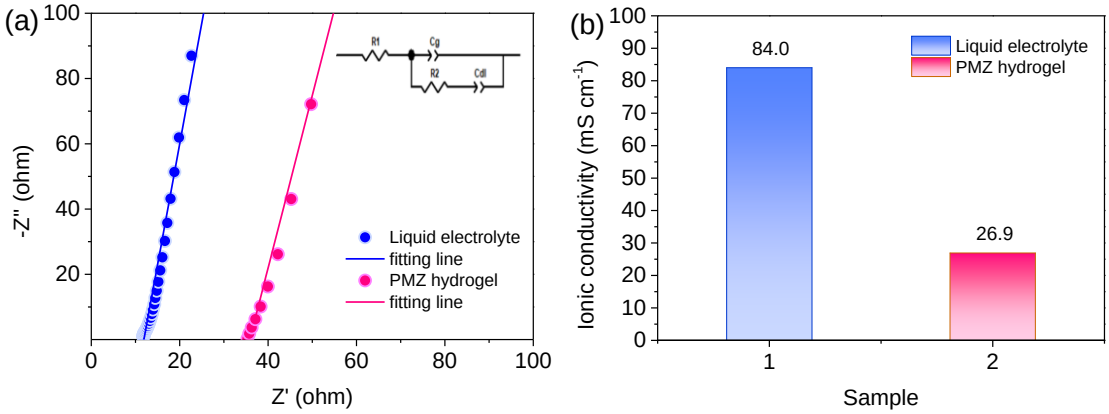

Figure S14. (a) Nyquist plots for the calculation of ionic conductivity. The insertion is the equivalent circuit. (b) Ionic conductivities.

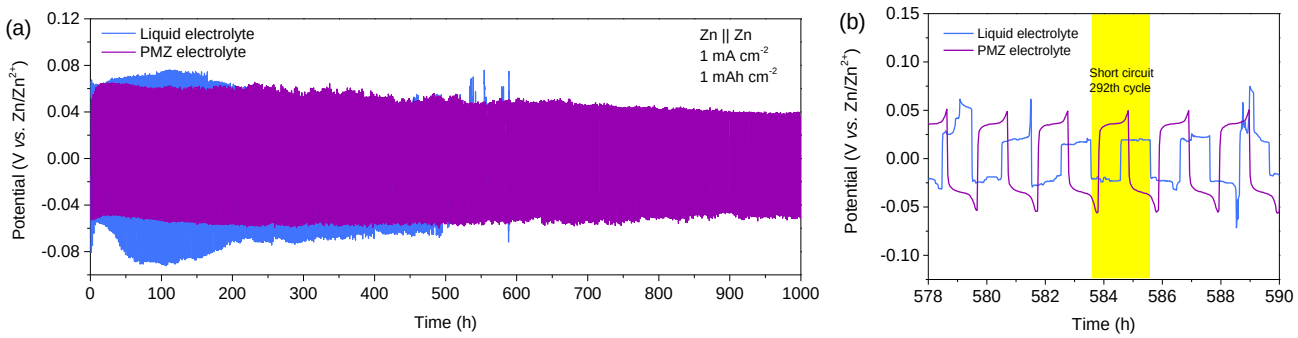

Figure S15. Electrochemical performance of Zn||Zn symmetric cells using different electrolytes under the current density/capacity of 1 mA cm^{-2}/1 mAh cm^{-2}. (a) Long-term potential profile and (b) potential profile around the 292th cycle.

The cycling performance of Zn||Zn symmetric cell using PMZ electrolyte presents the gradually decreased polarization under a higher current density and capacity of 1 mA cm^{-2} and 1 mAh cm^{-2}, which is ascribed to dendrite dissolution by fast ion transport under a high current density, resulting in a transient uniform deposition, indicating a gradually stabilized deposition/stripping on Zn foils [26]. The overpotential decreases after 500 times platting/stripping, demonstrating a gradually stable deposition process. The symmetric cell based on liquid electrolyte becomes short circuit since 292th cycle, which is ascribed to the contact of two pieces of Zn foils via the oriented growth dendrite.

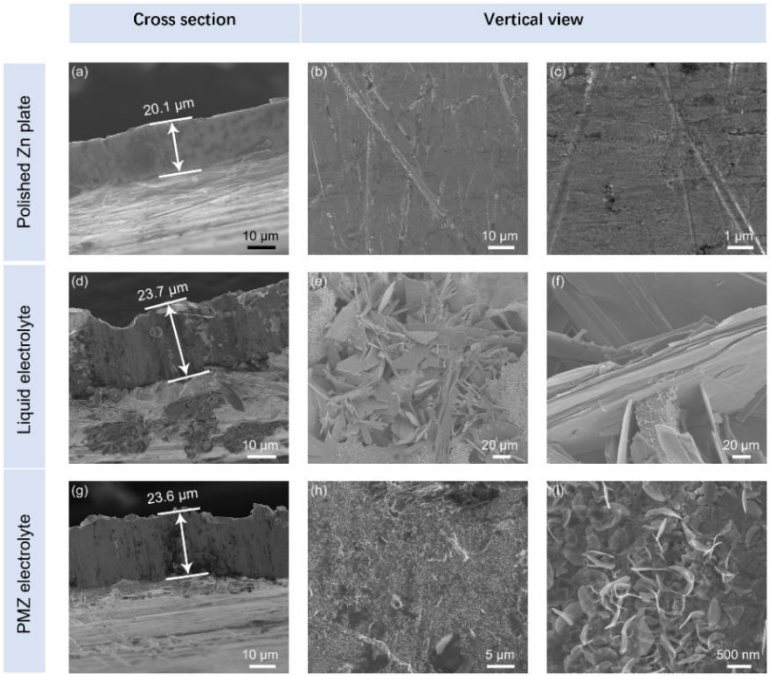

Figure S16. SEM images of electrodeposited Zn plates after Zn||Zn battery test with different electrolytes at 1 mA cm^{-2}. (a-c) Polished Zn foil. Zn foils using (d-f) liquid electrolyte and (g-i) PMZ electrolyte.

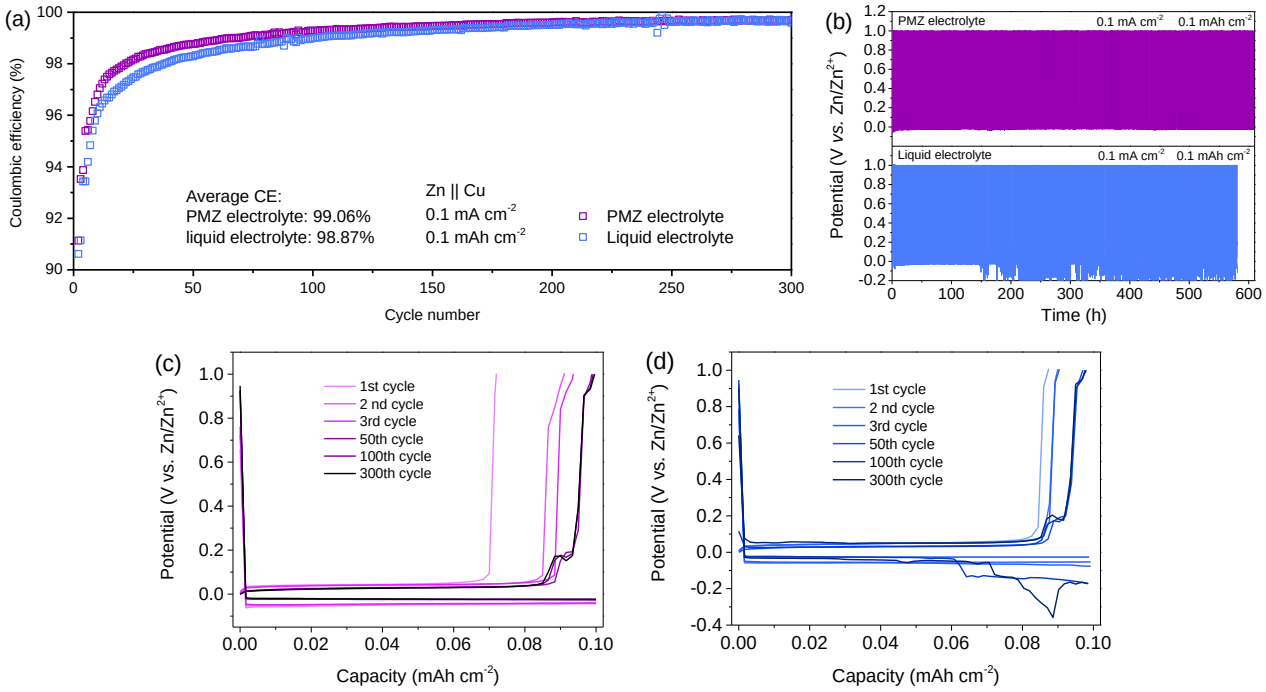

Figure S17. Polarization profiles of Zn||Cu asymmetric cells using different electrolytes at 0.1 mA cm^{-2} and 0.1 mAh cm^{-2}. (a) CEs, (b) potential-time profiles. Corresponding potential profiles of (c) PMZ electrolyte and (d) liquid electrolyte.

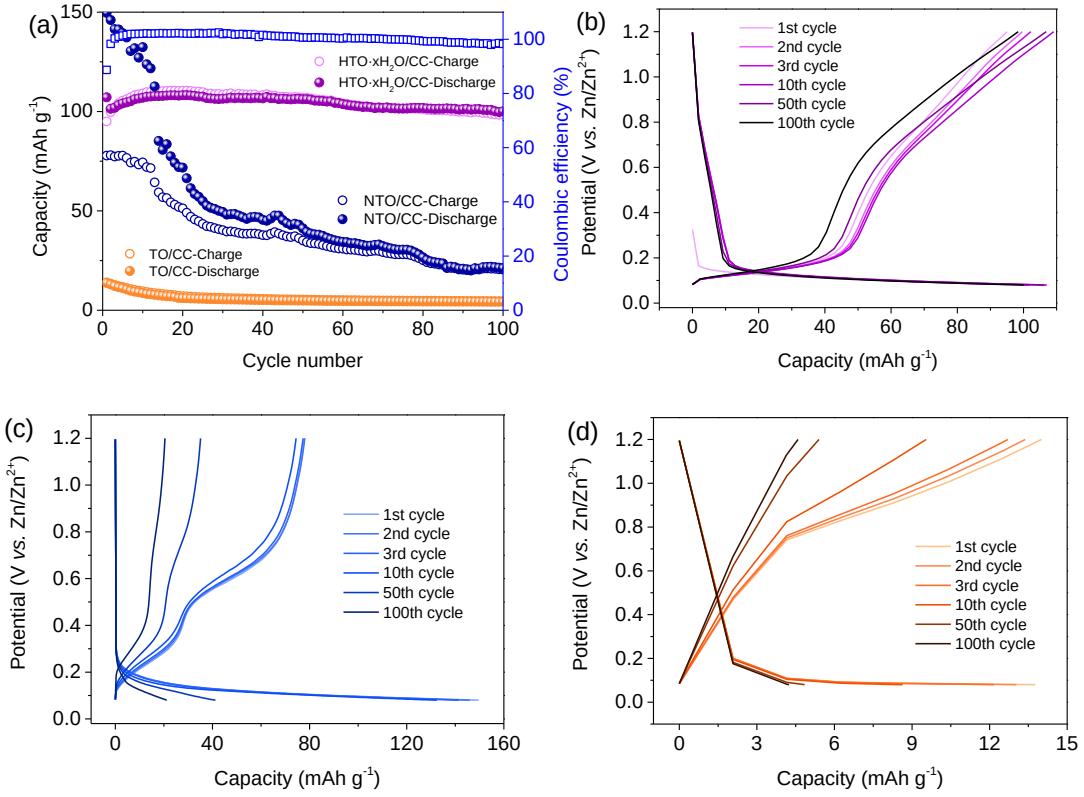

Figure S18. Electrochemical analyses at the current density of 0.1 A g^{-1}. (a) Cycling performance and corresponding charging-discharging curves of (b) HTO·xH2O/CC, (c) NTO/CC and (d) TO/CC.

The cyclic reversibility of the batteries using TO/CC, NTO/CC and HTO·xH$_2$O/CC were further conducted under the current density of 0.1 A g^{-1}. As presented in Figure S18, HTO·xH$_2$O/CC displays an initial capacity of 107.1 mAh g^{-1} then stabilizes at 101.8 mAh g^{-1} in the subsequent cycles and finally maintained at 100 mAh g^{-1} over 100 cycles, along with the CEs exceeding 99%. Whereas, NTO/CC shows a fast-decreasing trend from 149.6 mAh g^{-1} to 50 mAh g^{-1} since the 30th cycle and finally stabilized at 21.1 mAh g^{-1} over 100 cycles. TO/CC delivers low capacity of 4.2 mAh g^{-1} after 100 cycles, indicating a poor capability in Zn^{2+} storage.

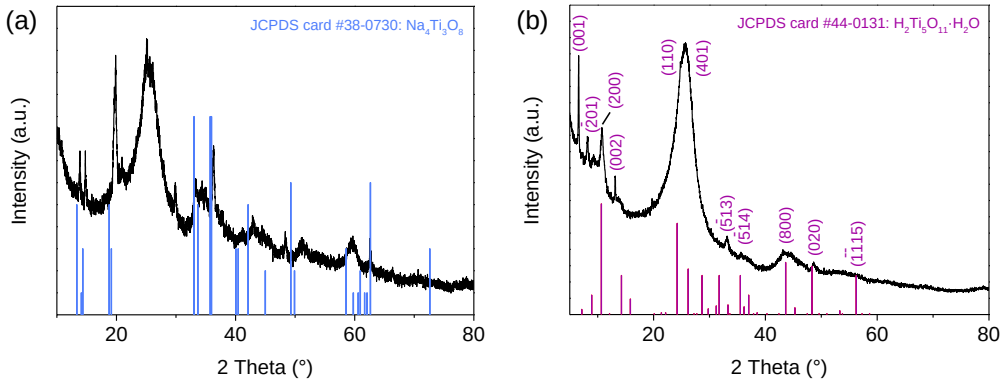

Figure S19. XRD patterns of post-cycled electrodes. (a) NTO/CC, (b) HTO·xH$_2$O/CC.

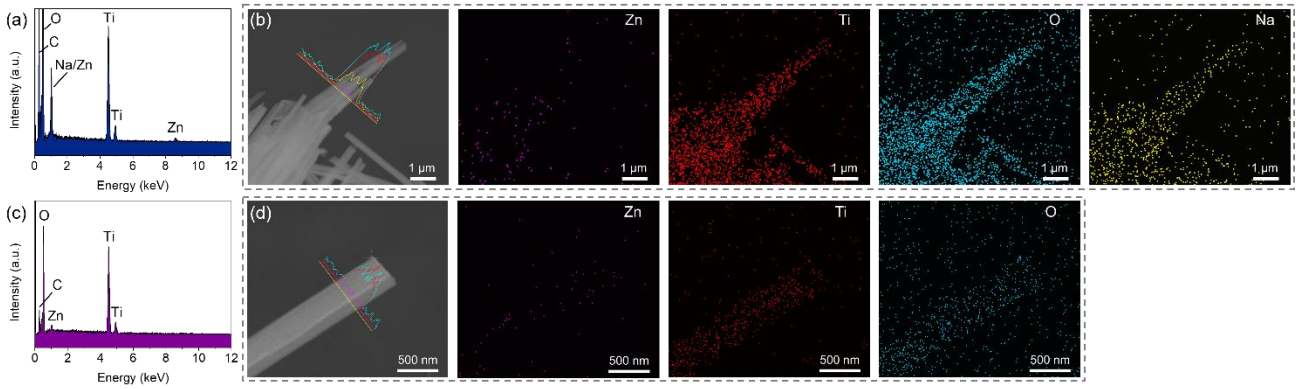

Figure S20. (a) EDS spectrum and (b) Elemental mapping of post-cycled NTO/CC electrode. (c) EDS spectrum and (d) Elemental mapping of post-cycled HTO·xH$_2$O/CC electrode. The insertion in each SEM image is line-scanning profile.

As for NTO anode, the high capacity in the initial period is attributed to Na^+ ions deintercalation from the interlayers of NTO, making it hard to return to the lattice. The diffraction peaks for post-cycled NTO/CC (onset voltage =1.2 V) slightly shift to positive direction, indicating the narrowing of lattice spacing, which is owing to the lattice contraction resulting from Na^+ irreversible dissolution (Figure

S19a). The XRD pattern of post-cycled HTO·xH$_2$O/CC displays the same composition compared to the fresh one (Figure S19b). EDS and elemental mapping images in Figure S20 further validate the reversibility after Zn^{2+} intercalation/deintercalation in HTO·xH$_2$O/CC.

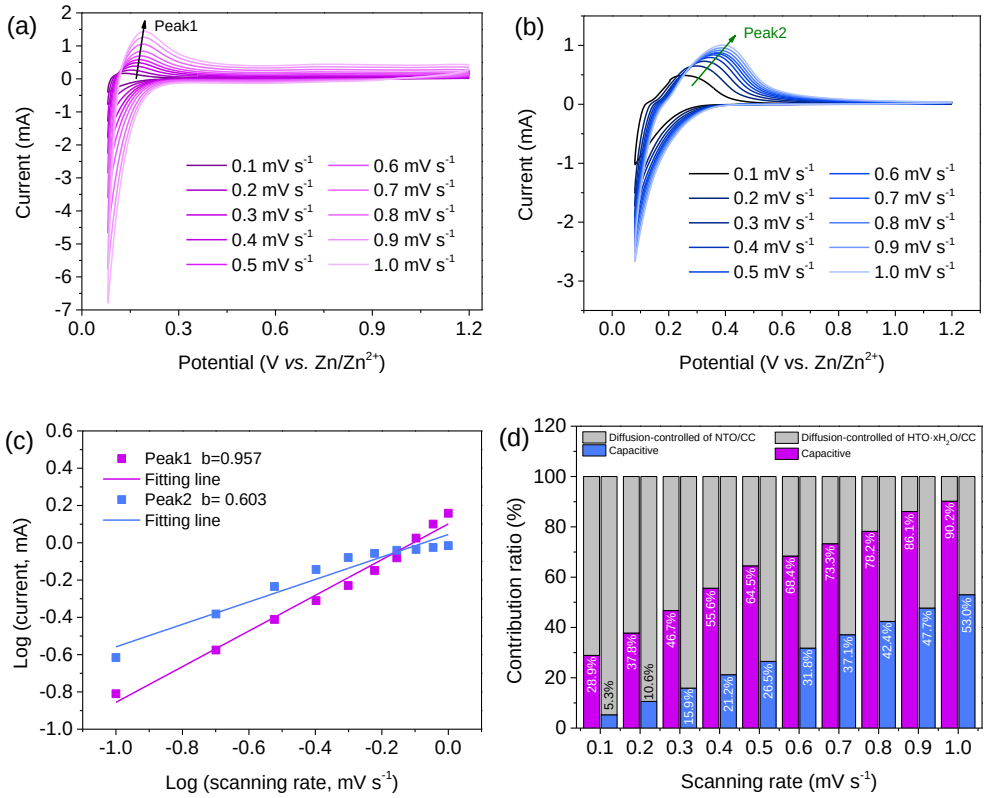

Figure S21. CV curves at various scan rates for different electrodes. (a) HTO·xH$_2$O/CC, (b) NTO/CC. (b) The relationship between logarithm of peak current and logarithm of scan rate, (c) contribution ratios of capacitive and diffusion-controlled.

The pseudocapacitive contribution ratios of anodic peaks for HTO·xH$_2$O/CC and NTO/CC were also measured (Figure S21). Depending on the increase of scanning rate, the capacitive contribution of HTO·xH$_2$O/CC shows an upward trend. The pseudocapacitive is dominated by a non-Faradic process (capacitive-controlled) with the scanning rate $\geq$ 0.4 mV s^{-1}. Therefore, the anodic processes are determined by surface redox reactions, which is beneficial for the enhancement of rate-performance and extension of lifespan under high current densities [27].

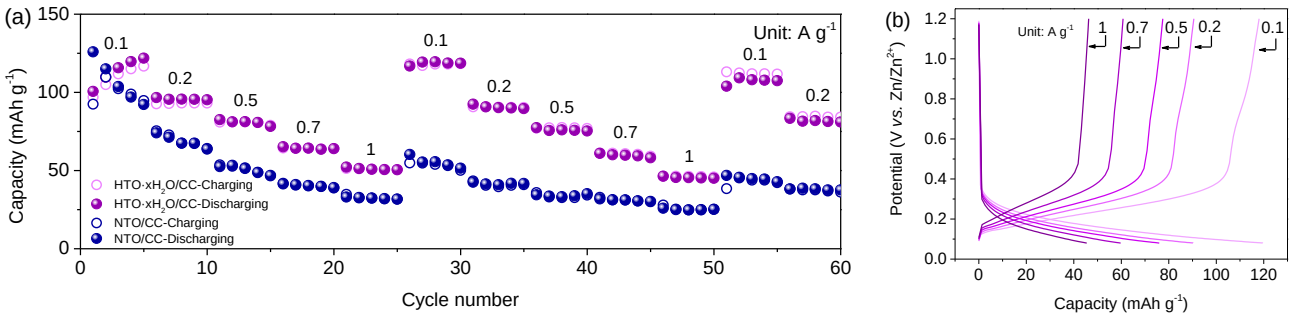

Figure S22. Rate performance of HTO·xH2O/CC and NTO/CC at various current densities. (b) galvanostatic charging-discharging curves of HTO·xH2O/CC for the second-round test.

In Figure S22, HTO·xH2O/CC anode delivers charging capacities of 118.0, 90.5, 77.4, 60.7 and 46.3 mAh g^{-1} under the current densities of 0.1, 0.2, 0.5, 0.7 and 1.0 A g^{-1} during the second-round test, along with a capacity retention rate of 96.8%, 95.0%, 95.7%, 94.8% and 91.7% compared to the first around. Whereas, the capacity retention rates for NTO/CC electrode are 47.9%, 57.4%, 65.6%, 76.8% and 78.3% under the same current densities. The low retention rate at 0.1 A g^{-1} is ascribed to Na^+ dissolution. The long-term cycling performance of HTO·xH2O/CC and NTO/CC anodes were conducted under the current density of 1 A g^{-1}.

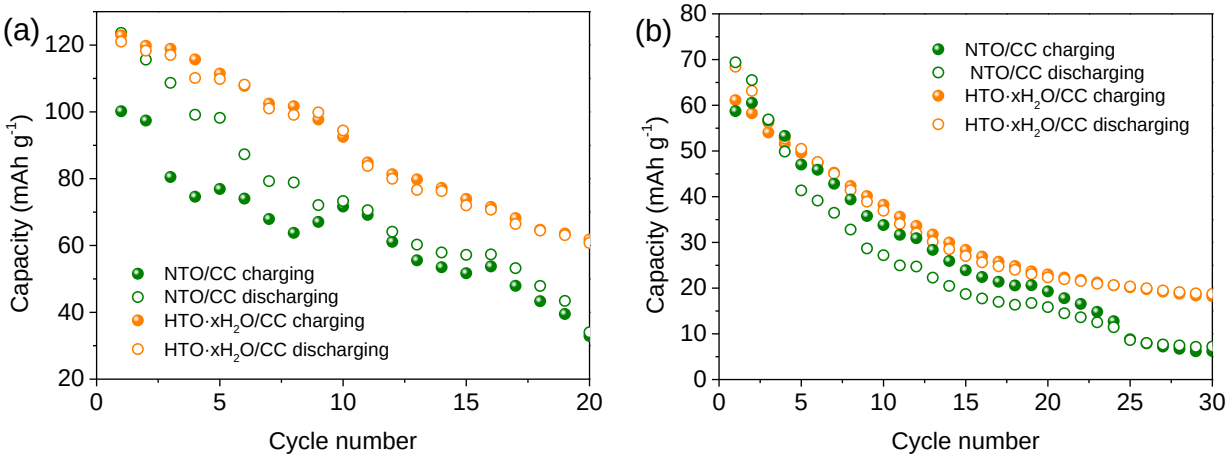

Figure S23. Batteries performance of HTO·xH2O/CC and NTO/CC by using 1 M $Zn(CF_3SO_3)_2$ liquid electrolyte under different current densities. (a) 0.2 A g^{-1}, (b) 1 A g^{-1}.

The performance of NTO/CC and HTO·xH2O/CC were measured by assembling 2032-type cells where Zn foils (thickness = 10 μm), glass fibers and 1 M $Zn(CF_3SO_3)_2$ solution were employed as anode, separator and liquid electrolyte. The consumption of liquid electrolyte was 200 μL for each cell.

As shown in Figure S23a, after 20 times cycling, HTO·xH2O/CC anode delivers the capacity of 60.7 mAh g^{-1}, along with the capacity retention of 50.2%. NTO/CC delivers a fast decreased capacity

from 123.6 mAh g^{-1} to 34.0 mAh g^{-1}, which is ascribed to the dissolution of Na^+ ions, resulting in irreversible capacity loss. The batteries show poor performance under high current density of 1 A g^{-1}. The capacity of HTO·xH2O/CC anode decreased from 68.4 to 18.7 mAh g^{-1} after 30 times cycling, while NTO/CC delivers the capacity from 69.4 to 7.2 mAh g^{-1}. The fast decreased performance are attributed to the uniform, deposition and side reactions, which are result from electrolyte consumption and Zn passivation.

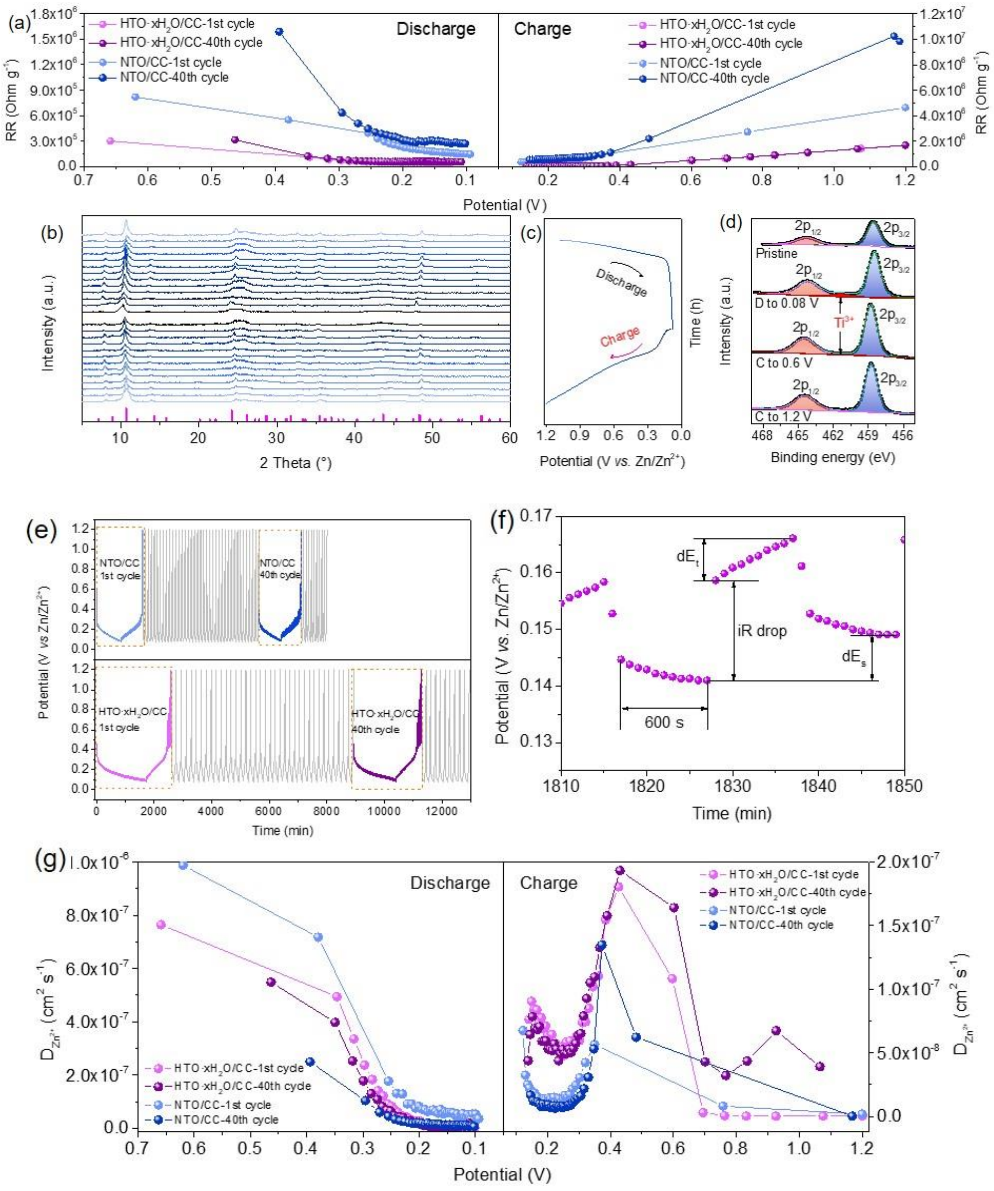

Figure S24. (a) Reaction resistance (RR) of NTO/CC and HTO·xH2O/CC calculated by GITT at the 1st and 40th cycles. (b) XRD patterns of HTO·xH2O/CC at various potentials and (c) galvanostatic charging/discharging (GCD) curves. (d) High-resolution XPS spectra of Ti 2p at the chosen potential. (C and D are abbreviations for charging and discharging, respectively.) (e) Potential-time curves during

GITT measurement. (f) Illustration of dE_s, dE_t and iR drop. (g) Diffusion coefficients under various potentials for the initial cycle and 40th cycle.

In Figure S24e, the cells by using HTO·xH$_2$O /CC and NTO/CC anode were cycled for 50 cycles, in which the 1st cycle and the 40th cycle are set for GITT test. As displayed in Figure S24f, dE_s is the difference of steady state potential and dE_τ is the variation of potential during pulse time. In our study, the pulse time and relaxion time were both set as 600 s.

$$D_{Li^+} = \frac{4}{\tau\pi}\left(\frac{n_m V_m}{S}\right)^2 \left(\frac{\partial E_s}{\partial E_\tau}\right)^2$$

$$RR=\Delta U/(I/m^2)$$

According to the above formula, the RR range of NTO/CC is 1.49×10^5~8.21×10^5 Ω g^{-1} in the initial discharge cycle, while the RR raises to 2.72×10^5~1.58×10^6 Ω g^{-1} after 40 cycles. Compared with the RR of HTO·xH$_2$O/CC in the discharging process (1st cycle: 5.12×10^4~3.03×10^5 Ω g^{-1} and 40th cycle: 5.83×10^4~3.17×10^5 Ω g^{-1}), the lowered RR at 0.08 V of NTO/CC is ascribed to the Na^+ participating in the ionic conductivity enhancement of hydrogel electrolyte. For the first cycle, the diffusion coefficient range of HTO·xH$_2$O/CC and NTO/CC are 7.64×10^{-7}~1.07×10^{-9} cm s^{-1} and 9.88×10^{-7}~3.62×10^{-9} cm s^{-1}, which is due to a fast Zn^{2+} insertion of NTO/CC. However, after 40 cycles, the coefficients for HTO·xH$_2$O/CC and NTO/CC are 5.49×10^{-7}~8.51×10^{-9} cm s^{-1} and 2.49×10^{-7}~6.40×10^{-9} cm s^{-1}, indicating the diffusion coefficient is dominated by Zn^{2+} intercalation/deintercalation after Na^+ dissolution reaches equilibrium. Therefore, low diffusion coefficient is owing to the Zn^{2+} storage space has occupied by irreversible Zn^{2+} insertion, leading to a slow kinetics.

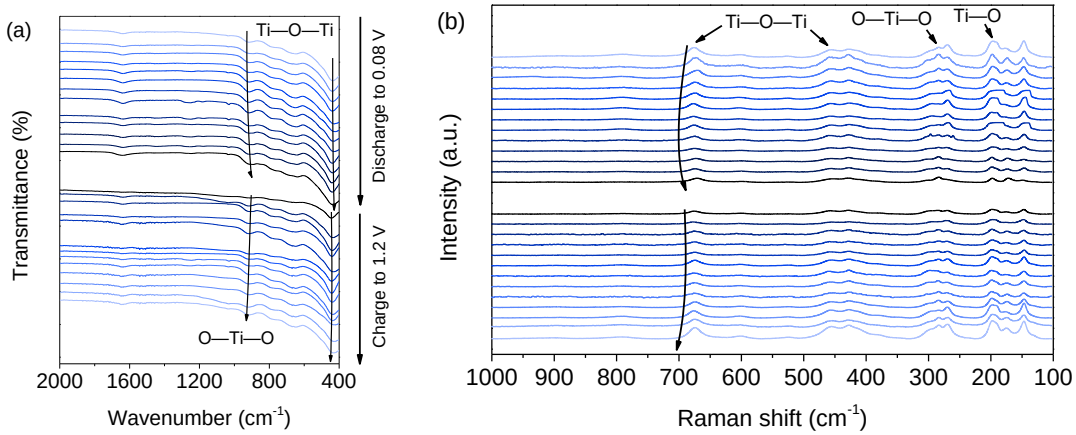

Figure S25. *Ex*-situ (a) attenuated total Refraction IR (ATR-FTIR) and (b) Raman spectra of HTO·xH$_2$O/CC at various potentials.

The Zn-storage mechanism of HTO·xH$_2$O/CC was studied by *ex*-situ ATR-FTIR, as displayed in Figure S24a. Two peaks located at 918 and 434 cm^{-1} are attributed to Ti—O—Ti and O—Ti—O vibration, respectively [28]. Two peaks shift to the lower wavenumber then move back during the

discharging/charging process, indicating a reversible intercalation/deintercalation of Zn^{2+} ions in HTO·xH$_2$O/CC anode [29]. Besides, the mechanism of HTO·xH$_2$O/CC anode was further investigated via *ex*-situ Raman spectra. As seen in Figure S24b, the doublet peaks located at 662 and 455 are assigned to the vibration of Ti—O—Ti, while another two peaks located at 283 and 195 cm^{-1} are attributed to the vibration of O—Ti—O and Ti—O, respectively [30]. When the battery discharge to 0.08 V, the Ti—O—Ti peak at 662 cm^{-1} negatively shift to small value, and the intensity become lower as well, it can be ascribed to the insertion of Zn^{2+} in HTO·xH$_2$O. In the subsequent charging process, the shifted peaks are returned to the standard position, indicating a reversible process of Zn^{2+} ions intercalation/deintercalation [31].

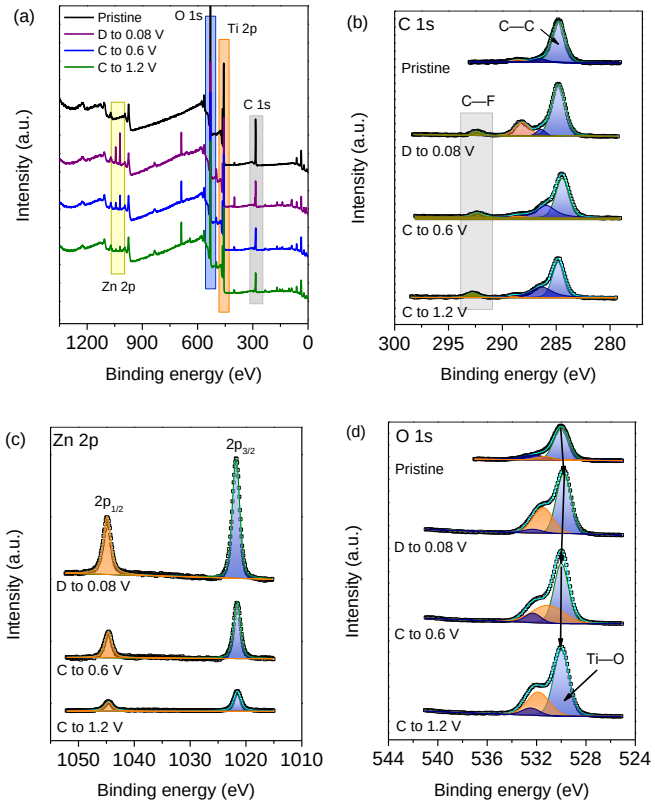

Figure S26. XPS spectra of HTO·xH$_2$O/CC at selected potentials. (a) XPS survey. High-resolution spectrum of (b) C 1s, (c) Zn 2p, (d) O 1s.

As seen from the survey spectrum (Figure S24a), Zn 2p, O 1s, Ti 2p and C 1s were employed to address the chemical state during charging/discharging process. All the data are calibrated by C–C peaks at 284.8 eV, as shown in Figure S24b. After battery cycling, a weak signal can be detected at ~292 eV can be indexed to C–F [32], which is attributed to the adsorption of $CF_3SO_3^-$ ions throughout the surface. Seen from Figure S24c, strong Zn 2p signal can be detected when the battery is discharged to 0.08 V, implying the intercalation of Zn^{2+}During the charging process, it can be observed a weakening trend of Zn 2p when the battery charging from 0.08 V to 0.6 V and finally cuts off at 1.2 V, indicating Zn^{2+}

deintercalation. In Figure S24d, it is noted the signal of Ti–O in O 1s spectrum shift from 530 (pristine) to 528.8 (D to 0.08 V) eV then back and stabled at 530.1 eV (C to 0.6 V and 1.2 V), demonstrating a reversible Zn^{2+} intercalation/deintercalation process [33].

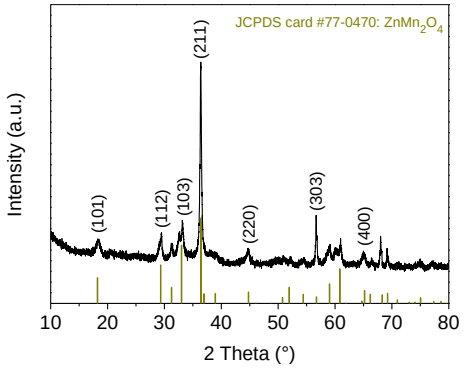

Figure S27. XRD pattern of ZMO/CC.

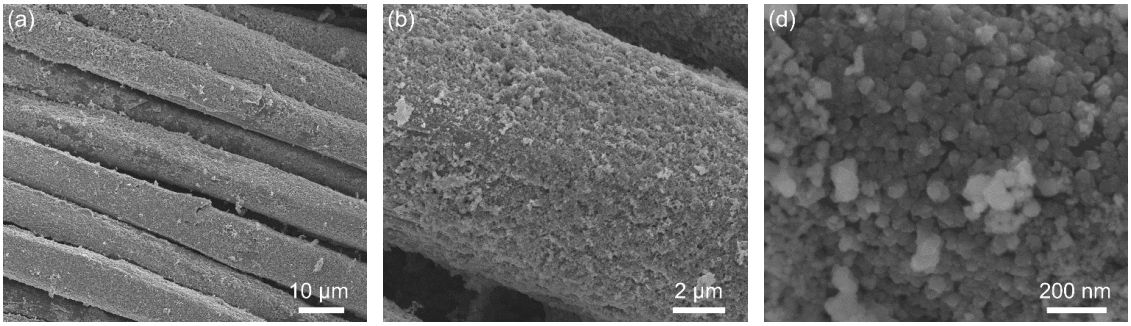

Figure S28. (a-c) SEM images of ZMO/CC at various magnification.

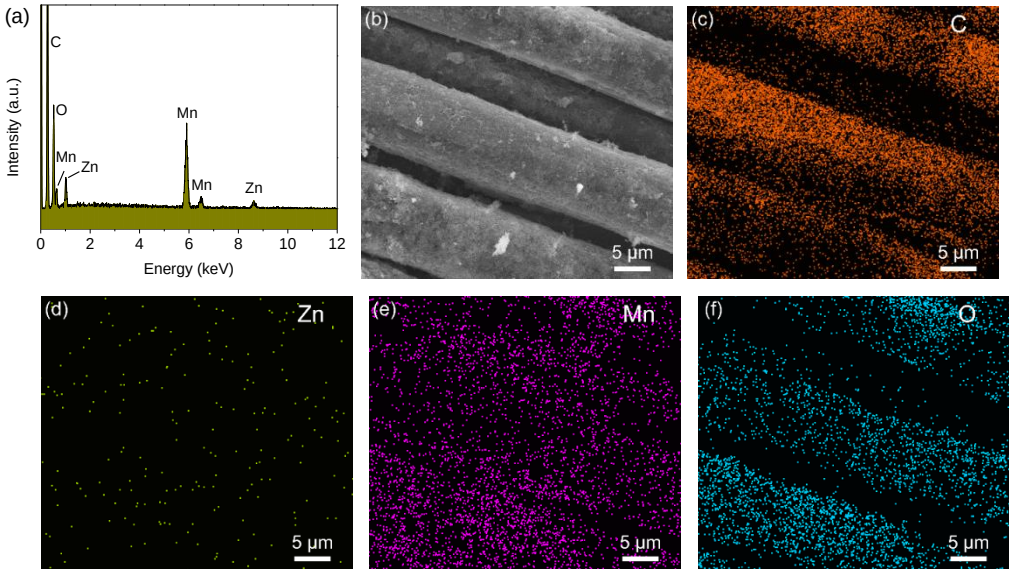

Figure S29. (a) EDS spectrum and elemental mapping images of ZMO/CC. (b) SEM image, (c) C, (d) Zn, (e) Mn, (f) O.

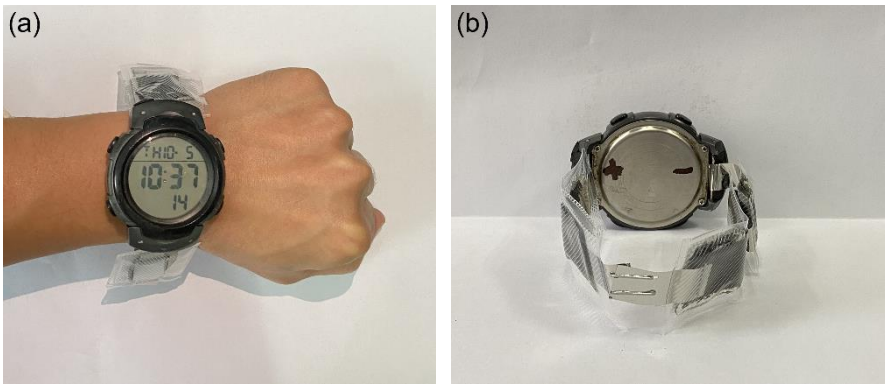

Figure S30. Optical photographs of the watch powered by the flexible batteries with ZMO/CC, HTO·xH$_2$O/CC and PMZ electrolyte as cathode, anode and electrolyte, respectively.

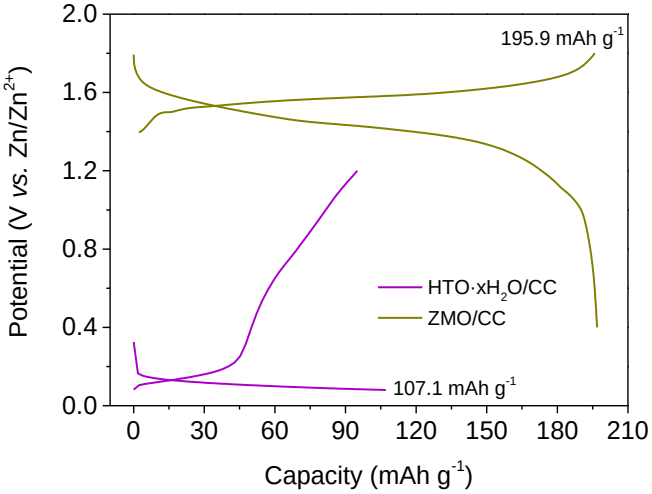

Figure S31. Charge and discharge curves of the HTO·xH$_2$O /CC and ZMO/CC with Zn plate at 100 mAh g^{-1}. The Zn^{2+} intercalation number (x) was calculated according to the discharge curve at 100 mAh g^{-1} and based on the following equation [34]:

$$C_0 = \frac{nF}{3.6M} \qquad x = \frac{nC_a}{2C_0}$$

where n refers to the number of theoretical electron exchange, C_a stands for the capacity in the charging (ZMO) or discharging process (for HTO), M($H_2Ti_5O_{11}$·4.1 H_2O)=491.3 g mol^{-1}, M($ZnMn_2O_4$)=239.3 g mol^{-1}, F=N_A×e=96485 C mol^{-1}, 1 Ah=3600 C).

Before battery assembly, ZMO/CC and HTO·xH$_2$O were cycled under 0.1 A g^{-1} versus the counter and reference electrode of Zn foils. For ZMO, the reaction Mn(III) → Mn(IV) occurs in the charging process, the theoretical capacity of ZMO can be calculated as 224.0 mAh g^{-1}, therefore, the Zn^{2+} ion deintercalation number can be calculated as 0.873. For HTO, the intercalation number can be calculated as 0.983 in terms of the same method with ZMO. According to the intercalation number and deintercalation numbers of HTO·xH$_2$O and ZMO/CC, the N/P ration is controlled as 1.83:1.

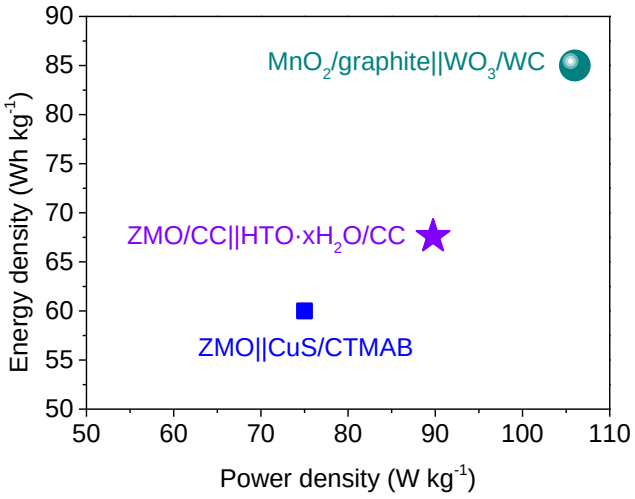

Figure S32. Ragone plots of the ZMO/CC||HTO·xH2O/CC cell, compared with previously reported rocking chair zinc-ion full batteries.

The obtained energy-power density of ZMO/CC||HTO·xH2O/CC was calculated based on the total weight of the cell. The cell delivers the energy density of 67.6 Wh kg^{-1} and powder density of 89.7 W kg^{-1}. Compared to some reported "rocking chair" AZIBs that MnO_2/graphite||WO_3/WC (85 Wh kg^{-1} under 106 W kg^{-1}) [35] and ZMO||CuS/CTMAB (60 Wh kg^{-1} under 75 W kg^{-1}) [36], the battery we reported is competitive.

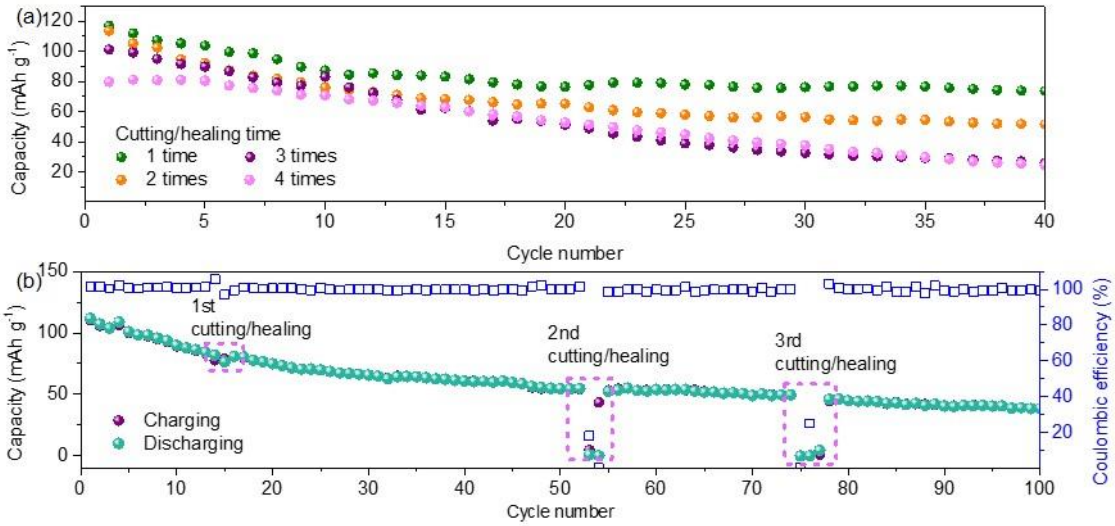

Figure S33. (a) Cycling performance after 1, 2, 3, and 4 repetitions of cutting and healing. (b) Cycling performance during the cutting and healing within 100 cycles.

Table S1. Comparison on the performance of Zn||Zn symmetric and Zn||Metal asymmetric using hydrogel electrolytes.

Hydrogel electrolyte	Zn||Zn symmetric cell			Zn||metal asymmetric cell			Ref.
	Current density/ mA cm^{-2}	Capacity/ mAh cm^{-2}	Lifespan/ h	Asymmetric cell	Capacity/ mAh cm^{-2}	Cycle numbers	
Carboxymethyl cellulose/polyacrylamide (CMC/PAM)	0.2	0.2	400	Not mentioned (N. M.)	N. M.	N. M.	37
PAM/CMC	1	1	4900	Zn||Cu	1	500	38
PAM/CMC/gelatin	0.1	0.1	1100	N. M.	N. M.	N. M.	39
Sorbitol-modified cellulose hydrogel	2	1	800	Zn||Cu	1	200	40
Guar-gum/sodium-alginate/ethylene-glycol hydrogel	0.2	N. M.	200	N. M.	N. M.	N. M.	41
PAM/LiBr/$LiNO_3$	0.5	0.25	500	Zn||Cu	0.5	200	42
Gelatin hydrogel	1	1	340	Zn||Ti	1	50	43
Gelatin hydrogel	1	0.5	1000	Zn||Cu	0.5	150	44
PMZ electrolyte	0.1	0.1	2000	Zn||Cu	1	600	This work
	1	1	1000				

Table S2. Comparison on some "Rocking chair" AZIBs using Zn metal-free anode.

Cathode	Anode	Current density/ A g^{-1}	Cycle number	Capacity/ mAh g^{-1}	Energy density/ Power density	Ref
MnO_2/graphite	WO_3/WC	0.1	100	69	85 Wh kg^{-1} 106 W kg^{-1}	35
$Zn_3V_4(PO_4)_6$	TiS_2	0.1	100	89.2	N. M.	45
$BiOIO_2$@$Zn_3(PO_4)_2$·4 H_2O	Mn_3O_4	0.1	1000	67	N. M.	46
$ZnMn_2O_4$	$H_2Ti_3O_7$·xH_2O	0.2	200	67	N. M.	47
Zn_xPVO (polyaniline	MoS_2@	2	2000	122.8	N. M.	48

intercalated V_2O_5)	ethylene glycol					
MnO_2	Co doped BiOBr	0.2	100	126	N. M.	49
MnO_2	Ni doped $Bi_2O_2CO_3$	0.05	80	100	N. M.	50
$ZnMn_2O_4$	CuS@CTMAB	0.1	100	211.1	60 Wh kg^{-1} 75 W kg^{-1}	36
$ZnMn_2O_4$	$Na_{0.14}TiS_2$	0.2	100	38	N. M.	51
$ZnMn_2O_4$/CC	$H_2Ti_5O_{11}·xH_2O$ /CC	0.1	60	64.3	67.6 Wh kg^{-1} 89.7 W kg^{-1}	This work

Reference

1 M. Kang, D. Won Kang, Y. Jun Yun, T. Kwon, D. Lee, K. S. Lim, C. S. Hong, *Chem. Eng. J.*, 2023, **470**, 144245.

2 Y. Shi, R. Wang, S. Bi, M. Yang, L. Liu, Z. Niu, *Adv. Funct. Mater.*, 2023, **33**, 2214546.

3 M. Yang, Y. Wang, D. Ma, J. Zhu, H. Mi, Z. Zhang, B. Wu, L. Zeng, M. Chen, J. Chen, P. Zhang, *Angew. Chem. Int. Edt.*, 2023, **62**, e202304400.

4 H. Yang, J. Huang, S. Liu, Y. Chen, Z. Cen, C. Shi, Y. Lu, R. Fu, *Small*, 2023, https://doi.org/10.1002/smll.202302537.

5 F. Niu, Z. Bai, Y. Mao, S. Zhang, H. Yan, X. Xu, J. Chen, N. Wang, *Chem. Eng. J.*, 2023, **453**, 139933.

6 J. Zhou, H. Zhao, N. Lin, T. Li, Y. Li, S. Jiang, J. Tian, Y. Qian, *J. Mater. Chem. A*, 2020, **8**, 6597-6606.

7 M. Winiecki, P. Krawczyk, *Chem. Eng. Sci.*, 2021, **237**, 116543.

8 S. C. Ray, D. K. Mishra, A. B. Panda, H. T. Wang, S. Bhattacharya, W. F. Pong, *J. Phys. Chem. C*, 2022, **126**, 8947-8952.

9 L. Liu, Y. Chen, J. Chen, W. Liu, G. Tang, H. Wen, Z. Xiao, S. Fan, *ACS Sustain. Chem. Eng.*, 2023, **11**, 5506-5514.

10 H. Pazniak, M. Benchakar, T. Bilyk, A. Liedl, Y. Busby, C. Noël, P. Chartier, S. Hurand, M. Marteau, L. Houssiau, R. Larciprete, P. Lacovig, D. Lizzit, E. Tosi, S. Lizzit, J. Pacaud, S. Célérier, V. Mauchamp, M. L. David, *ACS Nano*, 2021, **15**, 4245-4255.

11 J. Long, T. Han, X. Lin, Y. Zhu, Y. Ding, J. Liu, H. Zhang, *Nano Res.*, 2023, https://doi.org/10.1007/s12274-12023-15882-12279.

12 Y. Zhou, S. Zhang, M. A. Buckingham, L. Aldous, S. Beirne, C. Wu, Y. Liu, G. Wallace, J. Chen, *Chem. Eng. J.*, 2022, **449**, 137775.

13 K. Zhang, Y. Pang, C. Chen, M. Wu, Y. Liu, S. Yu, L. Li, Z. Ji, J. Pang, *Carbohydr. Polym.*, 2022, **293**, 119673.

14 B. Hua, L. Zheng, A. Adeboye, F. Li, *Chem. Eng. J.*, 2022, **443**, 136439.

15 D. Dhiman, A. S. C. Marques, M. Bisht, A. P. M. Tavares, M. G. Freire, P. Venkatesu, *Green Chem.*, 2023, **25**, 650-660.

16 S. Zhang, S. J. Kieffer, C. Zhang, A. G. Alleyne, P. V. Braun, *Adv. Mater.*, 2018, **30**, 1803140.

17 J. Conrad, P. R. Tremaine, *Phys. Chem. Chem. Phys*, 2021, **23**, 10670-10685.

18 S. Yun, S. Han, O. Borodin, D. M. Seo, T. Afroz, R. D. Sommer, W. A. Henderson, *J. Phys. Chem. C*, 2022, **126**, 18251-18265.

19 B. Dusolle, V. Jubera, E. S. Ilin, P. Martin, G. Philippot, M. R. Suchomel, B. B. Iversen, S. Marre, C. Aymonier,

Chem. Mater., 2023, **35**, 4057-4067.
20 T. Wei, Y. Ren, Z. Li, X. Zhang, D. Ji, L. Hu, *Chem. Eng. J.*, 2022, **434**, 134646.
21 H. Yu, H. Zhang, Z. Sun, Y. Wang, H. Liu, Y. Tong, L. Wu, J. Deng, L. Sun, *Chem. Eng. J.*, 2022, **450**, 138125.
22 Z. Kalaycıoğlu, B. Özuğur Uysal, Ö. Pekcan, F. B. Erim, *ACS Omega*, 2023, **8**, 13004-13015.
23 X. Ma, B. Liu, T. Ma, H. Zou, G. Chu, B. Sun, L. Zhang, Y. Luo, J. Chen, *Chem. Eng. Sci.*, 2021, **230**, 116216.
24 A. Crispini, M. La Deda, G. Di Maio, N. Godbert, A. Tagarelli, R. Elliani, A. Candreva, R. De Rose, I. Aiello, M. Amati, F. Scarpelli, *Cryst. Growth Des.*, 2023, **23**, 3518-3534.
25 S. Ansari, M. S. Ansari, S. P. Satsangee, R. Jain, *J. Pharm. Anal.*, 2021, **11**, 57-67.
26 Z. Xing, G. Xu, J. Han, G. Chen, B. Lu, S. Liang, J. Zhou, *Trends Chem.*, 2023, **5**, 380-392.
27 Q. Fu, B. Guo, W. Hua, A. Sarapulova, L. Zhu, P. G. Weidler, A. Missyul, M. Knapp, H. Ehrenberg, S. Dsoke, *Small*, 2023, https://doi.org/10.1002/smll.202304102.
28 L. A. García Contreras, J. O. Flores Flores, J. Á. Arenas Alatorre, J. Á. Chávez Carvayar, *J. Alloy Compds*, 2022, **923**, 166236.
29 Y. Deng, S. Dong, Z. Li, H. Jiang, X. Zhang, X. Ji, *Small Methods*, 2018, **2**, 1700332.
30 D. Zhao, X. Wang, W. Zhang, Y. Zhang, Y. Lei, X. Huang, Q. Zhu, J. Liu, *Adv. Funct. Mater.*, 2023, **33**, 2211412.
31 Y. Chen, D. Ma, K. Ouyang, M. Yang, S. Shen, Y. Wang, H. Mi, L. Sun, C. He, P. Zhang, *Nano-Micro Lett.*, 2022, **14**, 154.
32 M. Colin, S. Chen, H. Farhat, K. Guérin, M. Dubois, *Carbon*, 2023, **202**, 137-149.
33 S. Wang, Z. Yuan, X. Zhang, S. Bi, Z. Zhou, J. Tian, Q. Zhang, Z. Niu, *Angew. Chem. Int. Edt.*, 2021, **60**, 7056-7060.
34 T. Jiao, Q. Yang, S. Wu, Z. Wang, D. Chen, D. Shen, B. Liu, J. Cheng, H. Li, L. Ma, C. Zhi, W. Zhang, *J. Mater. Chem. A*, 2019, **7**, 16330-16338.
35 J. Cao, D. Zhang, Y. Yue, X. Wang, A. Srikhaow, C. Sriprachuabwong, A. Tuantranont, X. Zhang, Z. S. Wu, J. Qin, *Chem. Eng. J.*, 2021, **426**, 131893.
36 Z. Lv, B. Wang, M. Ye, Y. Zhang, Y. Yang, C. C. Li, *ACS Appl. Mater. Interfaces*, 2022, **14**, 1126-1137.
37 Y. Mao, H. Ren, J. Zhang, T. Luo, N. Liu, B. Wang, S. Le, N. Zhang, *Electrochim. Acta*, 2021, **393**, 139094.
38 R. Wang, H. Zhang, Y. Hu, R. Wang, J. Shen, Y. Mao, Q. Wu, B. Wang, *Electrochim. Acta*, 2023, **459**, 142583.
39 C. Jia, X. Zhang, S. Liang, Y. Fu, W. Liu, J. Chen, X. Liu, L. Zhang, *J. Power Sources*, 2022, **548**, 232072.
40 Y. Quan, W. Zhou, T. Wu, M. Chen, X. Han, Q. Tian, J. Xu, J. Chen, *Chem. Eng. J.*, 2022, **446**, 137056.
41 J. Wang, Y. Huang, B. Liu, Z. Li, J. Zhang, G. Yang, P. Hiralal, S. Jin, H. Zhou, *Energy Storage Mater.*, 2021, **41**, 599-605.
42 S. Lv, T. Fang, Z. Ding, Y. Wang, H. Jiang, C. Wei, D. Zhou, X. Tang, X. Liu, *ACS Nano*, 2022, **16**, 20389-20399.
43 L. Luo, Y. Liu, Z. Shen, Z. Wen, S. Chen, G. Hong, *ACS Appl. Mater. Interfaces*, 2023, **15**, 29032-29041.
44 Y. Yang, H. Lyu, Q. Wang, F. Mushtaq, X. Xie, F. Liu, X. Bo, W. Li, W. A. Daoud, *J. Mater. Chem. A*, 2023, **11**, 12373-12383.
45 D. Zhao, S. Chen, Y. Lai, M. Ding, Y. Cao, Z. Chen, *Nano Energy*, 2022, **100**, 107520.
46 Y. Qian, X. Li, H. Wang, T. Song, Y. Pei, L. Liu, X. Wang, Q. Deng, X. Wu, B. Long, *ACS Appl. Mater. Interfaces*, 2023, **15**, 17757-17766.
47 Y. Liu, X. Zhou, X. Wang, G. Chen, R. Liu, Y. Ma, Y. Bai, G. Yuan, *Chem. Eng. J.*, 2021, **420**, 129629.
48 Z. Lv, Y. Tan, Y. Kang, J. Yang, X. Cheng, W. Meng, Y. Zhang, C. C. Li, J. Zhao, Y. Yang, *Sci. China Chem.*, 2023, **66**, 1537-1548.
49 B. Long, Q. Zhang, T. Duan, T. Song, Y. Pei, X. Wang, C. Zhi, X. Wu, Q. Zhang, Y. Wu, *Adv. Sci.*, 2022, **9**, 2204087.
50 M. Han, Y. Qian, X. Li, N. Wang, T. Song, L. Liu, X. Wang, X. Wu, M. Law, B. Long, *J. Colloid Interface Sci.*,

2023, **645**, 483-492.
51 W. Li, K. Wang, S. Cheng, K. Jiang, *Adv. Energy Mater.*, 2019, **9**, 1900993.